Finite Element model of concrete repaired by High Molecular Weight Methacrylate (HMWM)

K. Ji[a,*], N. Gao[a], P. Wang[a], L. Stewart[a], C. Arson[a]

[a]*School of Civil and Environmental Engineering, Georgia Institute of Technology, USA*

Abstract

Epoxy is widely used to fill concrete cracks that are less than a millimeter in width to protect the steel rebars from corrosion. However, the mechanical behavior of epoxy-repaired concrete remains vastly unknown. In order to understand whether or not epoxy can be used to recover the mechanical properties of damaged concrete, we provide a quantitative assessment of concrete repaired by injection of High Molecular Weight Metacrylate (HMWM). Uniaxial compression tests and three-point bending tests were conducted on cut-and-repaired specimens. The experiments were simulated with the Finite Element Method (FEM), in which concrete was assigned a constitutive model that combines continuum damage mechanics and plasticity and in which the concrete/HMWM interface was modeled with bilinear softening cohesive zone elements (CZEs). The numerical model was calibrated and validated against the experimental results. Steel-reinforced concrete (RC) beams were subjected to three-point bending to produce cracks. The beams were then repaired and reloaded. We used Digital Image Correlation (DIC)

*Corresponding author.
E-mail address: kji9@gatech.edu
Phone: 404-680-0806

to identify the zones of high maximum principal strain after the first loading cycle. These zones were modeled with repaired concrete elements and HMWM CZEs to simulate the second load cycle. The load-displacement curves, damage distributions and strain fields obtained numerically are in agreement with those obtained experimentally, which validates the proposed model. Our simulation results suggest that HMWM can penetrate cracks of width 0.01 mm and above by gravity. We also found that HMWM reparation increases concrete stiffness and strength if crack in concrete members are over 0.1 mm in width, in which case, the load capacity of repaired RC beams is 30 to 40% higher than that of as-built RC beams.
Keywords: Concrete, reparation, epoxy, compression test, three-point bending test, Finite Element Method, Cohesive Zone Model, Concrete Damage Plasticity (CDP), Digital Image Correlation

1. Introduction

In order to reduce the carbon footprint of concrete infrastructure, it becomes necessary to design reparation techniques that can be applied based on simple criteria such as crack size and location [1]. Crack sealers are primarily used to clog cracks and avoid the steel rebars to be exposed to the atmosphere. In the State-of-the-Practice, the local application of sealants is viewed as a good way to repair shrinkage cracks in the early stages of crack propagation. However, the mechanical behavior of repaired concrete remains vastly unknown.

Sealants are commonly used as joints in pavements [2] or as water absorbers in concrete, to facilitate curing [3]. Sometimes, sealants are encapsu-

lated in brittle inclusions and liberated upon inclusion breakage, to seal the newly formed cracks [4, 5]. Penetrating hydrophobic sealers have long been considered of interest for construction. Wohl [6] highlighted the need for an experimental method to assess these hydrophobic sealers but did not explain how to conduct repeatable, standard physical tests. Mangnum and collaborators [7] were among the first to assess the use of polymers for repairing concrete. Several reparation and rehabilitation techniques, including the use of sealants, were then compared [8]. Unfortunately, the only sealants studied were salines and siloxanes, which were found to under-perform epoxies in later studies. Sprinkel [9] estimated the service life of several sealants solely based on the permeability of the sealed concrete. They noted that more data was needed to assess the skidding resistance of the repaired concrete decks. Recommendations on how to apply sealants in situ were provided in a Virginia Department of Transportation report [10]. Attanayake and collaborators proposed to measure the performance of silanes and siloxanes as a function of the permeability and durability of the repaired concrete, which they related to the depth of sealant penetration in concrete [11]; the study does not mention the friction properties of the concrete deck. An extensive literature review of deck sealants and crack sealants [12] concluded that standard epoxies and High-Molecular-Weight-Methacrylate (HMWM) were the best-performing sealants: standard epoxies allow recovering flexural strength but can only be injected in larger cracks, while HMWM can efficiently penetrate narrow cracks and reduce the permeability of concrete. These conclusions are supported by recent studies investigating the sealing potential of HMWM for concrete bridge decks [13] and for concrete airfield pavements

[14]. Liang tested four sealants *in situ*, on a bridge deck, and ranked their performance according to their ability to maintain a high skidding resistance, prevent chloride concentration increase in the treated concrete, prevent moisture transfer to the steel reinforcements and avoid temperature gradients in the treated concrete [15].

Because most studies focus on the transport of water and ions in concrete pores, less is known about the mechanical behavior of concrete repaired by epoxy or HMWM. Issa and Debs [16] tested fifteen concrete cubes in compression: six damaged concrete cubes without resin, six damaged concrete cubes repaired with epoxy resin, three intact (as-built) concrete cubes. The damaged concrete cubes had 32.71% to 40.93% less compressive strength than the intact samples. By injecting epoxy, the concrete strength was recovered by 50% with respect to its damaged (non-repaired) strength. Basunbul et al. [17] assessed epoxy remediation techniques by testing reinforced concrete beams. Only major cracks (larger than 0.3mm) were repaired by epoxy adhesives, while fine cracks were not repaired. It was found that repaired beams experience 50% less deflection than non-repaired beams and that epoxy injection does not increase the ultimate load of the damaged beam. However, similar tests conducted on three specimens by Dry and collaborators [18] showed that the load capacity of repaired concrete beams is on average equal to 133% of that of non-repaired concrete beams. As of now, there is no standard method to test concrete structural members repaired by epoxy.

This paper provides a quantitative assessment of concrete repaired by injection of a common epoxy used in construction: High Molecular Weight Metacrylate (HMWM). In the following, the terms epoxy and HMWM are

used interchangeably. A novel Finite Element model that combines continuum damage mechanics and cohesive fractures is calibrated against laboratory experiments done on plain and repaired concrete. The study concludes on which cracks to repair in order to restore the mechanical properties of a damaged structural member. Section 2 describes the uniaxial compression tests and three-point bending tests conducted on plain concrete specimens and on cut-and-repaired specimens, as well as the three-point bending tests performed on steel-reinforced beams. Digital Image Correlation (DIC) is used to calculate the strain field on one face of the beams before and after reparation. The proposed Finite Element model is presented in Section 3. The calibration and validation of the FEM model are explained in Section 4. Section 5 presents a series of simulations of three-point bending tests done on as-built and repaired reinforced concrete (RC) beams. After validating the model, we analyze the sensitivity of the mechanical response of the RC beam to the width of the cracks repaired. Lastly, Section 6 summarizes the main conclusions.

2. Experimental study of HMWM-repaired concrete

2.1. Materials and methods

2.1.1. Materials

The concrete mixture was prepared according to the specifications of the Georgia Department of Transportation (GDOT) [19] with the weight proportions listed in Table 1. We used a cement of type I and the concrete was made with a water-cement ratio of 0.47. We used coarse aggregates of size 67 from Norcross, Georgia, supplied by Vulcan Materials Company.

Table 1: Concrete mix used in the experiments.

Materials	Weight fraction (%)	Details
Cement	18.6	Type I
Water	5.3	
Fine Aggregate	28.3	Specific Gravity = 2.69
Coarse Aggregate	47.8	Specific Gravity = 2.71

The epoxy used for the repairs was the Sealte T-70 High Molecular Weight Methacrylate (HMWM) supplied by Transpo Industries, Inc. This HMWM is made of Cobalt Naphthenate, Cumene hydroperoxide, and resin, mixed in the proportions 75mL: 150mL: 3140mL, respectively. HMWM properties provided by the supplier are listed in Table 2. Additionally, we used published experimental data [20] for HMWM elastic moduli (also reported in Table 2).

We built steel-reinforced concrete (RC) beams that contained two #6 60 ksi steel rebars. Standard steel properties, listed in Table 3, were assumed in our simulations.

The laboratory tests conducted in this study are described in Table 4, and are described in the following paragraphs.

2.1.2. Splitting tests (Brazilian tests)

We performed eight Brazilian tests to measure the tensile strength of plain concrete. Specimens used in the Brazilian tests were cylinders 150mm in diameter and 300mm in height. The average indirect tensile strength of concrete (noted f_{its} in the following) was found to be 2.46MPa. Micro-

Table 2: HMWM properties.

Properties given by Transpo	
Unit weight of glassy state	$1.03g/mL$
Tensile strength	$> 11MPa$
Shear strength	$> 14MPa$
HMWM/concrete interface strength	$> 4.2MPa$
Properties reported in [20]	
Young's modulus (glassy state, ambient temperature)	0.95 GPa
Elongation (ASTM D 638)	10%

crack initiation depends on the real-tensile strength (noted f_{rts}), which itself depends on the indirect tensile strength measured for a characteristic length (noted l_1), according to the following relation [21]:

$$f_{its} = \frac{f_{rts}}{-17.57 + 66.05\dfrac{D_c}{l_1}} + 1.01305 f_{rts}, \qquad l_1 = \frac{E_c w_1}{2 f_{rts}} \tag{1}$$

Table 3: Steel properties.

Young's modulus	200 GPa
Yield tensile strength	420 MPa
Ultimate tensile strength	530 MPa
Ultimate tensile strain	0.1

Table 4: Summary of the experimental campaign

Experiment	Geometry of specimen	Numer of tests
Splitting test	D: 150 mm x H: 300 mm	8 as-built
Uniaxial compression test	D: 150 mm x H: 300 mm	6 as-built, 3 repaired
Three point bending tests:		
Non-reinforced beam	150 mm x 250 mm x 1200 mm	2 as-built, 2 repaired
(Notch depth)	(82 mm)	
Reinforced concrete beam	150 mm x 250 mm x 1200 mm	2 as-built, 3 repaired

where D_c is the diameter of the cylinder specimen and w_1 is the intercept of the initial tangent to the bilinear softening curve proposed by Elices and collaborators [22]. In the following, we used the real-tensile strength of concrete in order to account for strength scale effects [23]. The real-tensile strength of the 28-day concrete was found to be 2.26 MPa.

2.1.3. Uniaxial compression tests

Uniaxial compression (UC) tests were conducted on cylinders 150mm in diameter and 300mm in height. Concrete cylinders were cured and aged in a controlled fog room for 28 days. The HMWM-repaired concrete cylinders were fabricated by cutting plain concrete cylinders lengthwise on a tile cutter. Once cut, the faces of the two halves were ground flat in order to have a smooth surface for bonding. Construction silicon caulk was then applied to the edges of the sides of the two halves and a slim cardboard spacer was placed at the top and bottom to create a thin space ("crack"). The two halves were then pushed and tightened together using hose clamps, as illustrated in Figure 1. The silicon caulk was allowed to cure for 24 hours. The epoxy was

poured into the top opening of the sample until the newly constructed "crack" was completely filled with HMWM. The repaired concrete specimens were cured for at least 48 hours before testing. UC tests were conducted according to the ASTM C39 standards, for both the plain and repaired cylinders. A SATEC PRISM MKIII-C with the INSTRON 59-R7 controller was used to apply loading at 60 kips (420 MPa) per minute. The results of six test sets on plain concrete provided an average compressive strength of 35.54 MPa. Three tests were conducted on HMWM-repaired concrete, and the average compressive strength was 40.54 MPa. We calculated the Young's modulus of plain and repaired concrete based on the following equation [24]:

$$E_c = 5000\sqrt{f'_{co}} \quad \text{(unit: MPa)} \tag{2}$$

in which f'_{co} is the compressive strength. We found a Young's modulus of 28.52 GPa for plain concrete, and 31.82 GPa for repaired concrete. Note that Equation 2 was established for plain concrete. In the present study, we assume that the relationship holds for repaired concrete as well, based on empirical observations made in [25], in which the elastic modulus of repaired concrete cylinders was estimated through compressive strength tests.

2.1.4. Three-point bending tests on non-reinforced concrete beams

In order to analyze the mode I interfacial debonding behavior of plain and repaired concrete and measure the fracture energy of concrete before and after reparation, we conducted three-point bending (TPB) tests, following Hillerborg's recommendations [26]. The concrete beams were 1200 mm long with a cross section of dimensions 150 mm $\times$ 250 mm as shown in Figure 2. In the plain concrete beams, the notch was created by inserting a single

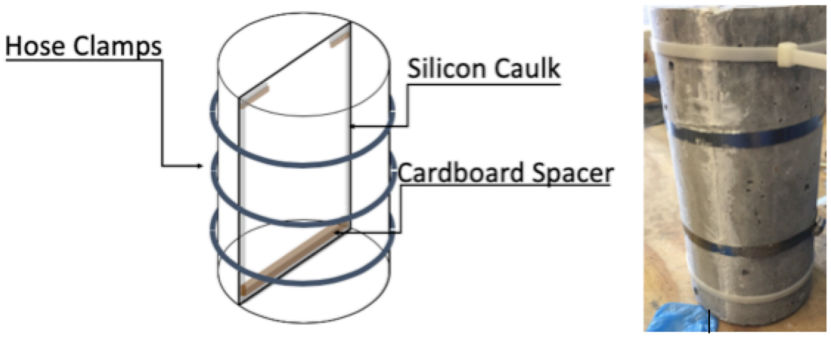

Figure 1: HMWM-repaired concrete specimens used in the uniaxial compression tests.

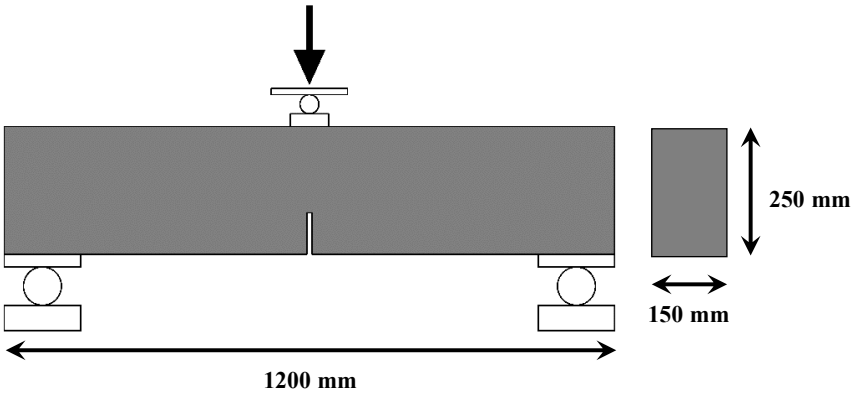

Figure 2: Geometry of the non-reinforced concrete beam specimens. The notch depth is 82 mm.

wall corrugated cardboard with a thickness of 3 mm and a depth of 82 mm. The HMWM-repaired beams were produced by cutting plain concrete beams in two halves with a masonry saw. A thin spacer was placed between the two halves, which were then reattached and sealed with silicon caulk. A corrugated cardboard 3 mm thick, 82 mm deep was placed in the thin space between the two halves. The silicon cured for 24 hours. Then HMWM was poured in the thin space and left in place to cure for 48 hours. Lastly, the corrugated cardboard was removed, to create a notch in the repaired beam.

A 50 kips (345 MPa) Interface 1220AO-50k load cell was employed to apply a load at a rate of approximately 2 kips (14 MPa) per minute. The crack mouth opening displacement (CMOD) was measured by means of a lateral variable differential transmitter (LVDT). We used a RDP DCTH200AG LVDT, with a maximum travel distance of $\pm$ 5 mm. Two non-repaired beams and two repaired beams were tested. The peak force of the HMWM-repaired beams was higher than that of the non-repaired beams. In both the plain and repaired specimens, vertical cracks propagated at the bottom of the beam (see Figure 3). In the repaired beams, the cracks formed within the concrete, and not at the interface between concrete and HMWM.

2.1.5. Three-point bending tests on steel-reinforced concrete beams

The reinforced concrete (RC) beams were fabricated with the same dimensions as the non-reinforced beams, without any initial notch. Two #6 steel rebars with a yield strength of 420 MPa were placed longitudinally as shown in Figure 4. We used a string potentiometer to measure the vertical displacement at the bottom center of the beams. Additionally, we speckled a longitudinal face of the beams and we measured the displacement field on

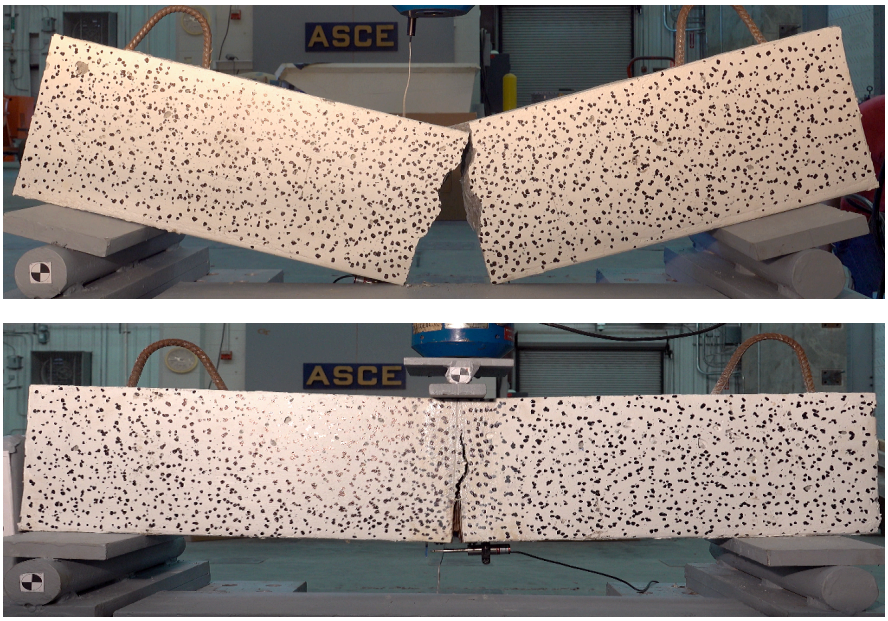

Figure 3: Non-repaired (top) and repaired (bottom) non-reinforced concrete beams after three-point bending tests.

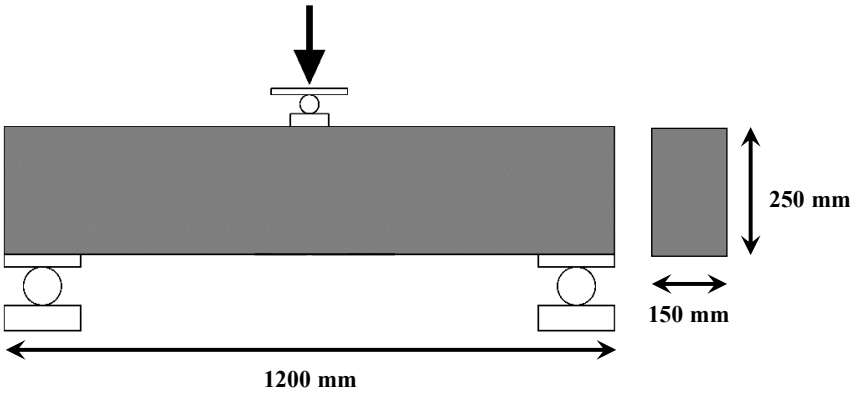

Figure 4: Geometry of the RC beam specimens. The rebars were placed at a distance of 45 mm from the bottom of the beam and the spacing between the rebars was 60 mm.

that face by using the Digital Image Correlation (DIC) software developed by Blaber and collaborators [27]. Two RC beams were tested "as built", to investigate the force-displacement behavior without HMWM injection. Three beams were loaded to develop different sizes of cracks (minor cracks obtained under a load of 80 kN or below, and major cracks obtained under a load of 100 kN). The three beams were then unloaded, removed from the load frame and laid on their sides. The change in orientation of the beam allowed gravity to assist the epoxy flow as it filled the cracks. HMWM was cured for at least 48 hours before testing. The cured repaired beams were then tested to failure with the same method as for the TPB tests done on non-reinforced beams. The displacement fields measured by DIC were post-processed to calculate the strain fields. The post-processed field of maximum principal strain is shown in Figure 5 for beams with minor and major cracks.

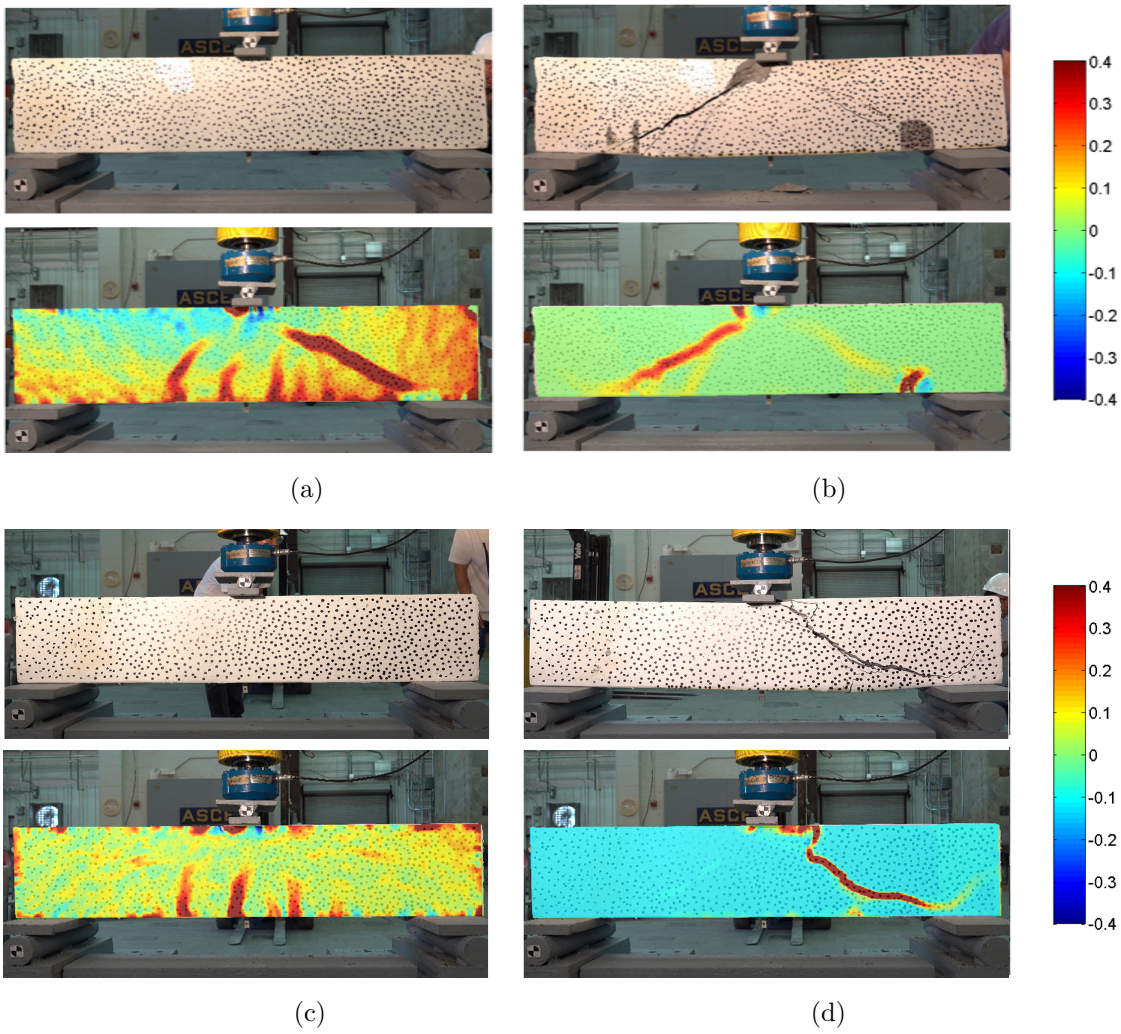

Figure 5: Photographs of the RC beams during the TPB tests and the corresponding field of maximum principal strain obtained by DIC (a) when major cracks developed (loading up to 100 kN); (b) when the beam with repaired major cracks failed; (c) when minor cracks developed (loading up to 80 kN); (d) when the beam with repaired minor cracks failed.

3. Finite element model

We simulated the experiments with ABAQUS/Explicit Finite Element software. An explicit dynamic solver was used to simulate the nonlinear behavior and failure mechanisms observed in the experiments. In order to overcome convergence issues that may occur in implicit formulations, we adopted a central-difference time integration scheme, in which the velocity and the acceleration at a particular time are considered constant at the next time step. The time increment was chosen so as to ensure that the internal strain energy remained below 5% of the total internal energy in all models, which avoided any dynamic artefact [28, 29]. Concrete was modeled with linear tetrahedral elements (C3D8). Cracks filled with epoxy were modeled with cohesive zone elements (COH3D8). The boundary conditions were the same as in the experiments. In the following, we give an overview of the constitutive models employed in the simulations.

3.1. Concrete model

We used the Concrete Damage Plasticity (CDP) model proposed by Lubliner and collaborators [30], and later improved by Lee and Fenves [31]. The CDP model couples the concepts of damage mechanics in elasticity with tensile and compressive plasticity to represent the inelastic behavior of concrete. Concrete stress-strain curves are represented in Figures 6a and 6b, for compression and tension, respectively. The stress-strain response in com-

pression is assumed to obey the following constitutive relationships [24]:

$$\begin{aligned} f_c &= \frac{f'_{cc} x r}{r - 1 + x^r}, \quad x = \frac{\varepsilon_c}{\varepsilon_{cc}} \\ \varepsilon_{cc} &= \varepsilon_{co}\left[1 + 5\left(\frac{\varepsilon_c}{\varepsilon_{cc}} - 1\right)\right] \\ r &= \frac{E_c}{E_c - E_{sec}}, \quad E_{sec} = \frac{f'_{cc}}{\varepsilon_{cc}} \end{aligned} \tag{3}$$

where f_c is the uniaxial compressive stress, ε_c denotes the strain under that stress, f'_{cc} is the compressive strength, and ε_{co} is a reference value set to 0.02. The compressive stress-strain curve is typically obtained point by point, by measuring the strain while controlling the stress, or vice versa. The tensile behavior of concrete is determined by a bilinear softening curve, which shows good agreement with the load-displacement curve obtained experimentally. In Figure 6b, w is the displacement. The stress ratio at the kink point (ψ) is set to 0.2, based on previous studies [32]. Both in tension and compression, the damaged behavior is captured by an equation of the form:

$$\boldsymbol{\sigma} = (1 - d)\boldsymbol{E_0}(\boldsymbol{\varepsilon} - \boldsymbol{\varepsilon_{pl}}) \tag{4}$$

where d is the damage variable (in compression or tension); $\boldsymbol{E_0}$ is the elastic-stiffness tensor; $\boldsymbol{\varepsilon}$ is the total strain; $\boldsymbol{\varepsilon_{pl}}$ is the plastic strain. The compressive and tensile inelastic deformation and damage parameters are typically obtained by performing uniaxial compression tests and splitting tests, respectively. The relationship between the damage and strain variables is calculated as follows [33]:

$$\begin{aligned} d_c &= 1 - \frac{\sigma_c}{E_0(\varepsilon_c - \varepsilon_c^{pl})} \\ d_t &= 1 - \frac{\sigma_t}{E_0(w_t - w_t^{pl})} \end{aligned} \tag{5}$$

in which the c subscript stands for compression, the t subscript stands for tension and the pl superscript stands for plastic. The fracture energy for the bilinear softening curve is calculated by using the following empirical relation [34, 35]:

$$G_f = 2.5^{-3}\beta_0 \left(\frac{f_c^{'}}{5.8^{-2}}\right)^{0.4} \left(1 + \frac{A_{max}}{1.94}\right)^{0.43} \left(\frac{w}{c}\right)^{-0.18} \tag{6}$$

where β_0 is an aggregate shape factor (1.12 for angular aggregates and 1 for rounded aggregates); f_c' is the compressive strength (MPa); A_{max} is the maximum aggregate size (mm); w/c is the water-cement ratio. On the basis of all the given concrete information, G_f was estimated as 0.105 N/mm in our experiments, which is within the range of expected values for standard concrete (0.084-0.13N/mm [35]). We calculated the damage parameters so as to fit the stress/strain curves obtained experimentally. We defined the tension softening behavior by applying the displacement method in ABAQUS. The tensile strength determined experimentally and the fracture energy calculated from the constitutive relationships presented above were first used to calculate the crack opening displacement at different levels of tensile stress. These displacements were then used to define the bilinear stress-crack opening displacement behavior in the CDP. This allowed us to capture the bilinear softening curve, as demonstrated also in other studies [36, 37]. Additional plasticity parameters include the dilation angle, the eccentricity parameter, the ratio f_{bo}/f_{co} and the coefficient K_c, respectively chosen as 30^o, 0.1, 1.12 and 0.75, based on previous studies [38, 39, 40, 41]. f_{bo} and f_{co} are concrete compressive strength under biaxial loading and uniaxial compressive strength, respectively. The coefficient K_c is the ratio of the second stress invariant on the tensile meridian of the failure surface to that on the com-

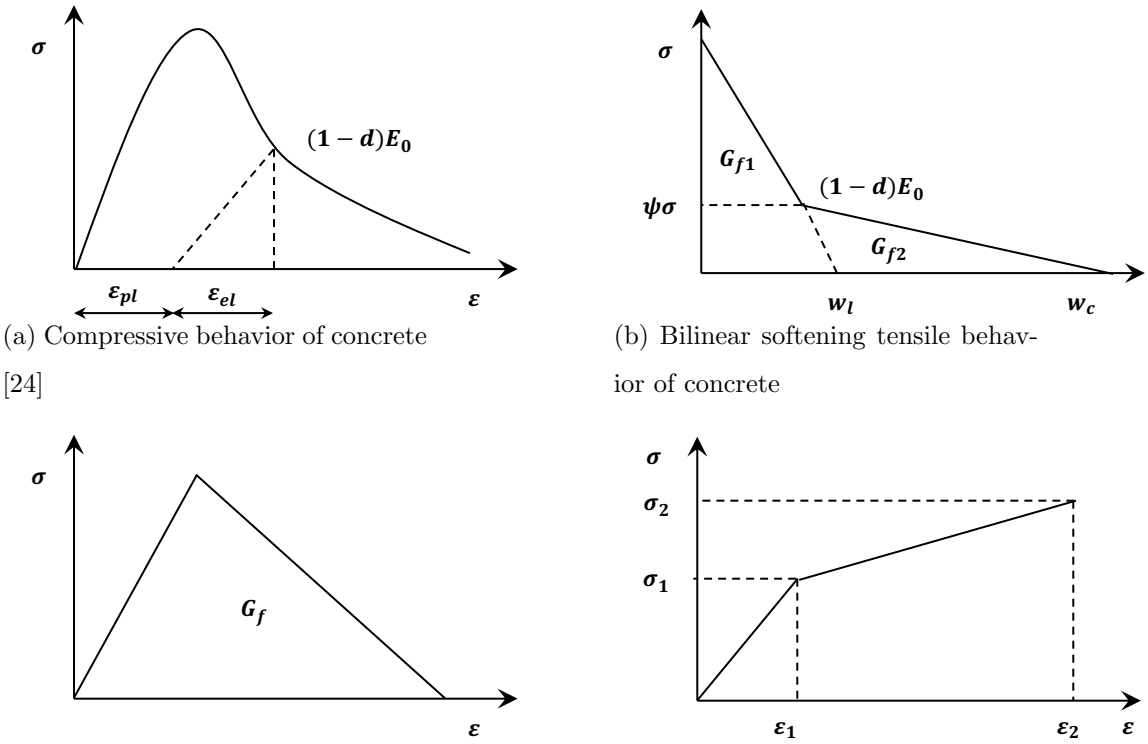

(a) Compressive behavior of concrete [24]

(b) Bilinear softening tensile behavior of concrete

(c) HMWM/concrete linear softening traction-separation law

(d) Stress-strain response of #6 60 ksi steel rebars

Figure 6: Material models used for FE simulation.

pressive meridian, given the first invariant of the volumetric stress tensor [42].

3.2. HMWM model

The cracks filled with cured epoxy (HMWM in the glassy state) were modeled with bilinear softening cohesive zone elements (CZE) both in tension and shear, as illustrated in Figure 6c. The traction-separation law used in ABAQUS is expressed in terms of nominal tractions and displacement, as

follows:

$$T = \begin{Bmatrix} t_n \\ t_s \\ t_t \end{Bmatrix} = \begin{bmatrix} k_{nn} & 0 & 0 \\ 0 & k_{ss} & 0 \\ 0 & 0 & k_{tt} \end{bmatrix} \begin{Bmatrix} \delta_n \\ \delta_s \\ \delta_t \end{Bmatrix} = K\delta \tag{7}$$

T is the traction force vector, with components in the normal direction (t_n), in the shear direction (t_s) and in the tangential direction (t_t). The cohesion stiffness tensors are noted k_{ii}, where i stands for n, s or t. $\boldsymbol{\delta}$ is the displacement vector, corresponding to nominal strains. The equilibrium equation and the compatibility condition in a laminated material are [43, 44]:

$$\begin{aligned} \sigma &= E_3\varepsilon = K\Delta \\ \varepsilon_{eff} &= \varepsilon + \frac{\Delta}{t} = \frac{\delta}{t} + \frac{\Delta}{t} \end{aligned} \tag{8}$$

where σ is the traction force, ε_{eff} is the effective strain of the laminate element, $\varepsilon = \dfrac{\delta t}{t}$ is the transverse strain (where t is the initial thickness of the joint), K is the interface stiffness and Δ is the opening displacement. Considering the constitutive condition $\sigma = E_{3eff}\varepsilon_{eff}$, the effective Young's modulus of the laminated material can be written as:

$$E_{eff} = E_3 \left(\frac{1}{1 + \dfrac{E_3}{K_t}} \right) \tag{9}$$

Because the cohesive stiffness should not affect the effective modulus of a sandwich laminate, the cohesive stiffness should satisfy $E_3 << K$. The equation can be expressed as:

$$k_{ss} = \frac{\alpha E}{t}, k_{ss} = k_{tt} = \frac{\alpha G}{t} \tag{10}$$

where α is much larger than 1. Consequently, we assigned k_{nn} and k_{ss} a value 50 times ($\frac{\alpha}{t} = 50$) larger than that of the Young's modulus and shear modulus (which was given as 0.95GPa) [20].

In the simulations, we used the strength parameters provided by the supplier (11 MPa in tension, 14 MPa in shear). We used a power law [45] to relate the critical tensile and compressive fracture energies and account for mixed-mode CZE debonding, as follows:

$$\left(\frac{G_n}{G_n^C}\right)^\alpha + \left(\frac{G_s}{G_s^C}\right)^\alpha + \left(\frac{G_t}{G_t^C}\right)^\alpha = 1 \tag{11}$$

where G_n^C, G_s^C, and G_t^C are the critical fracture energies to initiate fracture propagation in the tension, first shear, and second shear directions, respectively. The power-law parameter α was calibrated by simulating the UC tests (as explained in the following section). To ensure stability, we used a time increment smaller than the following critical time increment [46]:

$$\Delta t = T_c\sqrt{\frac{\rho_c}{E_c}} \tag{12}$$

where T_c is the thickness of the cohesive layer, E_c is the elastic modulus of HMWM and ρ_c is the density of HMWM.

3.3. Model for steel reinforcements

Rebars were modeled as truss elements embedded in the concrete FEs. We used a perfect bond condition between the concrete and steel elements. A bilinear hardening stress/strain curve describes the constitutive behavior of steel (Figure 6d).

4. Model calibration

The material parameters that could not be found in the literature or in the specifications given by the suppliers were calibrated to ensure that the force-displacement curves obtained numerically fit the experimental results. Note that in the simulations of repaired RC beams, we used repaired concrete Finite Elements in addition to the CZEs, i.e., Finite Elements with higher stiffness and strength than the plain concrete elements. Table 5 summarizes all the material parameters used in the Finite Element model, and explains how those parameters were found. Further details on the RC beam model are provided in Section 5. In the following, we explain our calibration simulations.

4.1. Uniaxial compression tests

We simulated the UC tests done in the laboratory. Plain concrete specimens were modeled with plain concrete FEs (which were assigned the CDP model) with a 5 mm mesh size. The repaired specimens were modeled in the same way, with HMWM cohesive zone elements assigned in a middle longitudinal plane. The rigid platens at the top and bottom of the specimen were modeled explicitly with rigid FEs. The interface between the specimen and the platen was modeled with a hard contact (non-penetrability condition), with a friction coefficient of 0.1 based on current standards [47]. Fixed displacements were imposed to the centroid of the bottom platen. The vertical displacement at the centroid of the top platen was increased until the ultimate axial compressive displacement was reached. We extracted the force and the displacement at the centroid of the top rigid platen during the UC

Table 5: Summary of the material parameters used in the FEM model.

Plain and repaired concrete elements		
Poisson's ratio	Standard value	0.2
ϵ_{c0}	Literature review [32]	0.02
ψ	Literature review [32]	0.2
dilation angle	Literature review [38, 39, 40, 41]	30^o
eccentricity	Literature review [38, 39, 40, 41]	0.1
f_{b0}/f_c	Literature review [38, 39, 40, 41]	1.12
K_c	Literature review [38, 39, 40, 41]	0.75
Plain concrete elements		
Young's modulus	From Eq. 2 and measured compression strength	28.52 GPa
Tensile strength	From experiments and Equation 1	2.28 MPa
Tensile fracture energy G_f	From experiments and Equation 6	0.105 N/mm
Repaired concrete elements		
Young's modulus	From Eq. 2 and measured compression strength	31.82 GPa
Tensile strength	Calibrated	7.6 MPa
Tensile fracture energy G_f	Calibrated	0.3 N/mm
Cured HMWM Cohesive Zone Elements		
Young's modulus	Literature review [20]	0.95 GPa
Poisson's ratio	Standard value	0.3
Cohesive stiffness	Standard practice: 50 times Young's modulus [20]	47.500 GPa
Tensile strength	Calibrated	8 MPa
Shear strength	Literature review [20]	14 MPa
Tensile fracture energy G_f	Calibrated	0.4 N/mm
Shear fracture energy $G_s = G_t$	Calibrated	1.2 N/mm
Exponent in power law α	Calibrated	1
CZE thickness	Calibrated	0.15 mm
Steel truss elements		
Young's modulus	Standard value	200 GPa
Yield tensile strength	Standard value	420 MPa
Ultimate tensile strength	Standard value	520 MPa
Ultimate tensile strain	Standard value	0.1

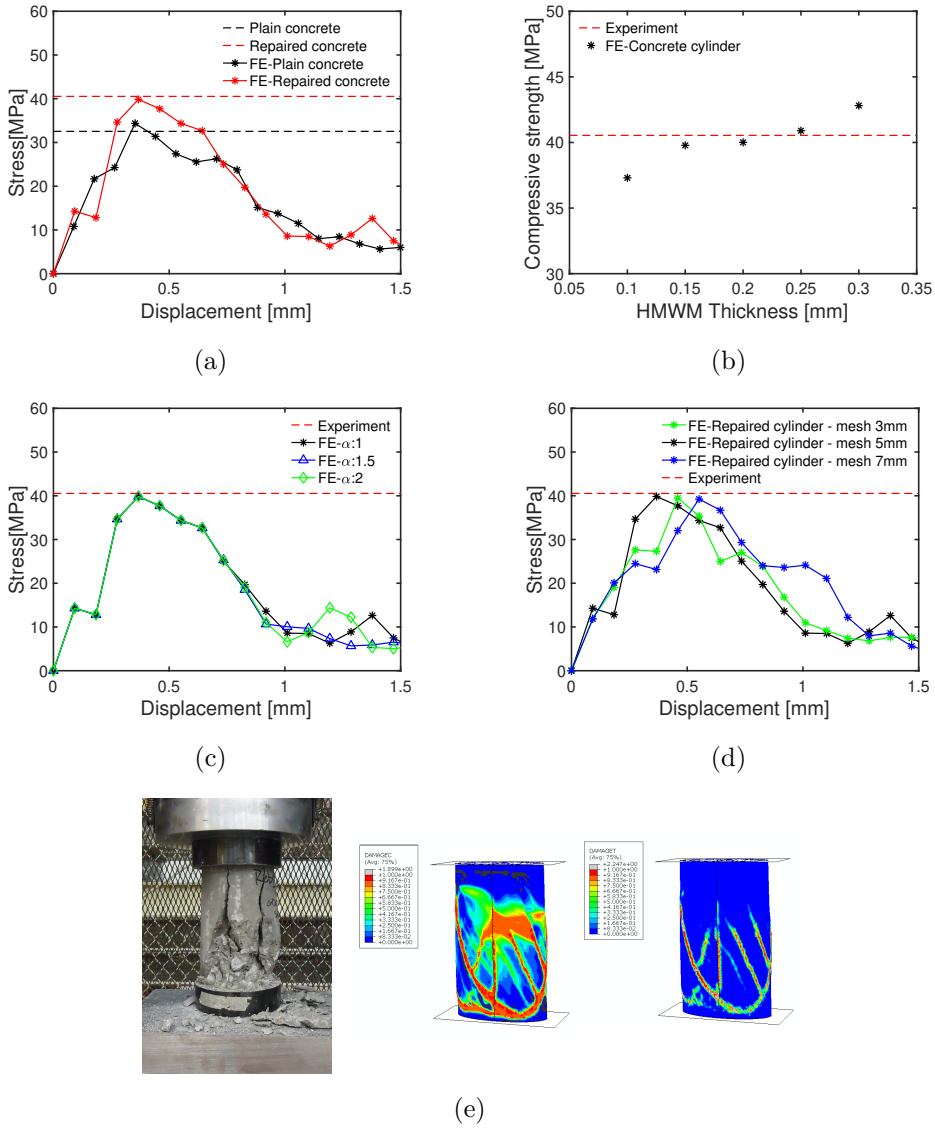

Figure 7: Comparison of numerical and experimental results for the UC test. (a) Stress-displacement curves obtained numerically, and strengths obtained experimentally. (b) Numerical strength of the repaired specimen for different CZE thicknesses. (c) Numerical stress-displacement curves obtained with repaired concrete specimens, for different values of the exponent α. (d) Stress-displacement curves obtained numerically for different mesh sizes. (e) Damage at the end of the UC test simulation in repaired concrete. From left to right: photograph of a fractured specimen; contour plot of simulated compressive damage on the outer surface; contour plot of simulated tensile damage on the outer surface; contour plot of simulated compressive damage in a section cut;contour plot of simulated tensile damage in a section cut.

test simulations. Figure 7(a) shows the vertical stress/displacement curves obtained numerically for the plain and repaired concrete specimens. For both types of specimen, the peak stress found numerically matches the compressive strength measured experimentally (32.54 MPa for plain concrete and 40.54 MPa for repaired concrete). Computational results indicate that the initial stiffness of plain concrete is lower than that of repaired concrete. Figure 7(b) and (c) show a parametric study of the CZE thickness and of the exponent parameter α. Based on these sensitivity analyses, we found that the best fit was 0.15 mm for the CZE thickness and 1 for the exponent α. The value of α is consistent with previous studies, which recommend a value of 1 for epoxy adhesive materials [48]. We analyzed the sensitivity of the model of UCT for repaired specimens to mesh size. We compared three different mesh sizes (3, 5, 7 mm). The three models predicted similar compressive strength values and stress-displacement curves, as shown in Figure 7(d). The distribution of damage in the repaired concrete specimen is shown in Figure 7 (e). The damaged zone obtained numerically is in good agreement with the fracture pattern observed experimentally during the UC tests: cracks appear mostly at the bottom of the specimen and along the reparation plane.

4.2. Three-point bending tests on non-reinforced concrete beams

In order to validate the model calibration done with the UC tests (with the parameters given in Table 5), we simulated TPB tests conducted on non-reinforced repaired concrete beams. The mesh is shown in Figure 8. Based on previous studies [49], we used a finer mesh size of 1 mm in the region of the expected crack path to avoid mesh sensitivity during simulations. Figure 9 compares the envelopes of the three load/Crack Mouth Opening Displace-

ment (CMOD) curves obtained experimentally to the load/CMOD curves obtained numerically. The numerical curves lie between the load/CMOD curves obtained experimentally, for both the plain and repaired beams. In other words, the model predicts a representative average behavior of plain and repaired concrete in tension. The behavior of the repaired beams was similar to that of the plain beams, with a slightly higher peak load (11.44 kN instead of 10.84 kN in the simulations). As expected, tensile damage propagates vertically ahead of the notch, within the concrete, along the crack plane filled with HMWM (i.e., along the CZEs) as shown in Figure 9.

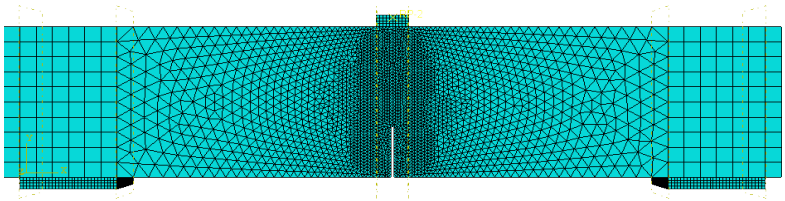

Figure 8: Geometry and mesh size of Finite Element models of three-point bending tests on non-reinforced concrete beams.

5. Application: reparation of reinforced concrete beams

5.1. Validation against experiments

We modeled the RC beams with 3D solid concrete elements with an edge size of 10 mm and two-node linear truss steel elements with a length of 10 mm. We simulated a TPB test with the parameters given in Table 5. The load-displacement curve obtained numerically is compared to the load-displacement curves obtained experimentally in Figure 11(a). Each RC beam had a speckled longitudinal face that was filmed during the TPB test. We

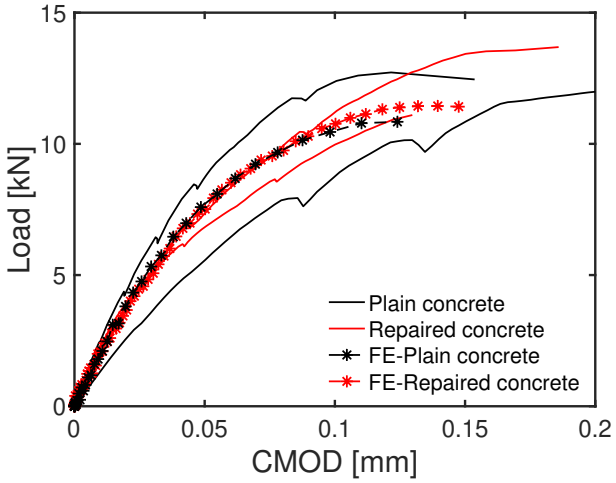

(a)

(b)

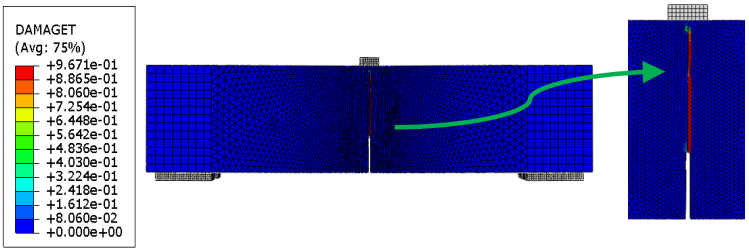

(c)

Figure 9: (a) Evolution of the Crack Mouth Opening Displacement during the TPB tests done on plain and repaired non-reinforced concrete beams: numerical predictions are representative of the average behavior observed experimentally. (b) Photograph of a failed specimen after three-point bending tests. (c) FE result of crack propagation within concrete during three-point bending tests.

used DIC to map the displacement field on those speckled faces. We then calculated the field of maximum principal strains. We found that cracks were present wherever the maximum principal strain exceeded 0.002. We used that threshold to define the damaged zone after the TPB tests, as illustrated in Figure 10. The contour of the damaged zone identified by DIC was then transformed into a binary image and meshed, by using the tracing image method in Solidworks. In that mesh, HMWM CZEs were insterted between all FEs, by using Truster's 3D interface element insertion code [50]. The volume elements were assigned the CDP model, with the properties of a "repaired" concrete, i.e. concrete with a larger stiffness, larger tensile strength and larger compressive strength than plain concrete (see Table 5). The "repaired concrete" elements represent concrete that contains small cracks filled with HMWM (i.e., cracks smaller than the fractures represented by the CZEs). The model thus accounts for the propagation and repair of both large cracks (of the order of 0.01 mm in width) and small cracks (less than 0.01 mm in width).

Out of the three repaired RC beams, two were loaded up to 100 kN and exhibited "major cracks" before reparation, and one was loaded up to 80 kN and exhibited "minor cracks" before reparation. We categorized cracks as minor or major depending on their crack width, which were calculated based on the following equation [51]:

$$w_{cr} = w_{bw}\left(\epsilon_p - \frac{\sigma_p}{E}\right) \tag{13}$$

where E is the Young's modulus of concrete, w_{cr} is the crack width and w_{bw} is the crack bandwidth, which is equal to the length of the edge of an element in the numerical model. ϵ_p and σ_p are respectively the maximum

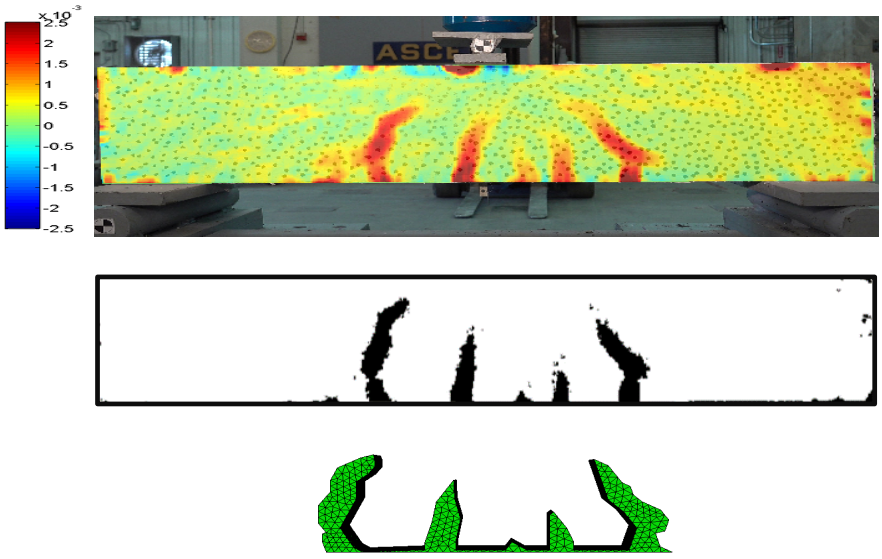

Figure 10: Method to identify the damaged zone after the TPB tests on RC beams. Top: the field of maximum principal strain is calculated by DIC. Bottom: the zone where the maximum principal strain exceeds 0.002 is binarized and meshed with SolidWorks.

principal strain and maximum principal stress, which were post-processed from the simulation results. We found that the major cracks (obtained when the beam was loaded up to 100 kN) had a width over 0.1 mm. For minor cracks (obtained when the beam was loaded up to 80 kN), the main crack width was less than 0.1 mm. We simulated the TPB tests on the three beams after reparation. Figure 11(b) shows that the numerical result predictions for repaired RC beams with major cracks are in good agreement with the experimental results up to the peak. After the peak, the two beams with major cracks exhibited very different experimental responses. We attribute the difference between the two experimental responses after reparation to differences in the crack patterns that were generated by loading prior to reparation. The numerical curve matches one of the two experimental curves. So overall, the numerical model performs satisfactorily. Figure 11(c) shows that the proposed model reproduces well the behavior of the repaired RC beam with minor cracks, which is actually very similar to that of as-built RC beams. We analyzed the sensitivity of the model of reinforced concrete beam to mesh size. We compared three mesh sizes (5, 10, 15 mm), as shown in Figure 11(d). Results indicate that the softening behavior occurs the earliest when the mesh size is 5 mm. According to previous studies and ABAQUS User's Manual [46, 52], in finer meshes, crack zones localize in regions where there is little or no reinforced concrete, which results in softening failure before extensive damaged zones develop. Mesh sizes of 10 and 15 mm provided load-displacement curves in agreement with experimental results. That is why we used a mesh size of 10 mm in all the RC beam simulations. Results show that the capacity of the repaired RC beams with major cracks was

approximately 40% higher than that of the as-built RC beams. This result suggests that epoxy injection could strengthen concrete with larger cracks with a width of 0.1mm and above, for which the specific area of contact between the concrete and HMWM is high.

The numerical model predicts crack or damage propagation in the zone where cracks were observed experimentally, and it predicts a maximum principal strain field in good agreement with that obtained by DIC (Figure 12). The model performs equally well for the specimens that had major cracks and for the specimens that had minor cracks. In particular, the model captures the occurrence of flexural and shear cracks at the same locations as in the experiments.

5.2. Sensitivity analyzes

We analyzed the sensitivity of the mechanical response of the repaired RC beams to the width of the cracks filled by epoxy. First, we simulated the TPB tests conducted on RC beams with loading up to 80 kN and up to 100 kN. Then, we post-processed the results to obtain the contours of the zones in which cracks had similar widths. We set different threshold widths for repair. For example, we first identified a target zone for repair in which all the cracks were 0.1 mm wide or larger. In that zone, we inserted CZEs and replaced the concrete FEs by repaired concrete FEs. Next, we simulated the TPB test again, and plotted the force displacement curve, which we compared to the force-displacement curve obtained experimentally for the as-built and repaired beams. Simulation results for a crack width threshold of 0.1 mm are presented in Figures 13 (a) and (b), where the grey zone in the mesh represents the target repair zone. For the RC beams loaded up to

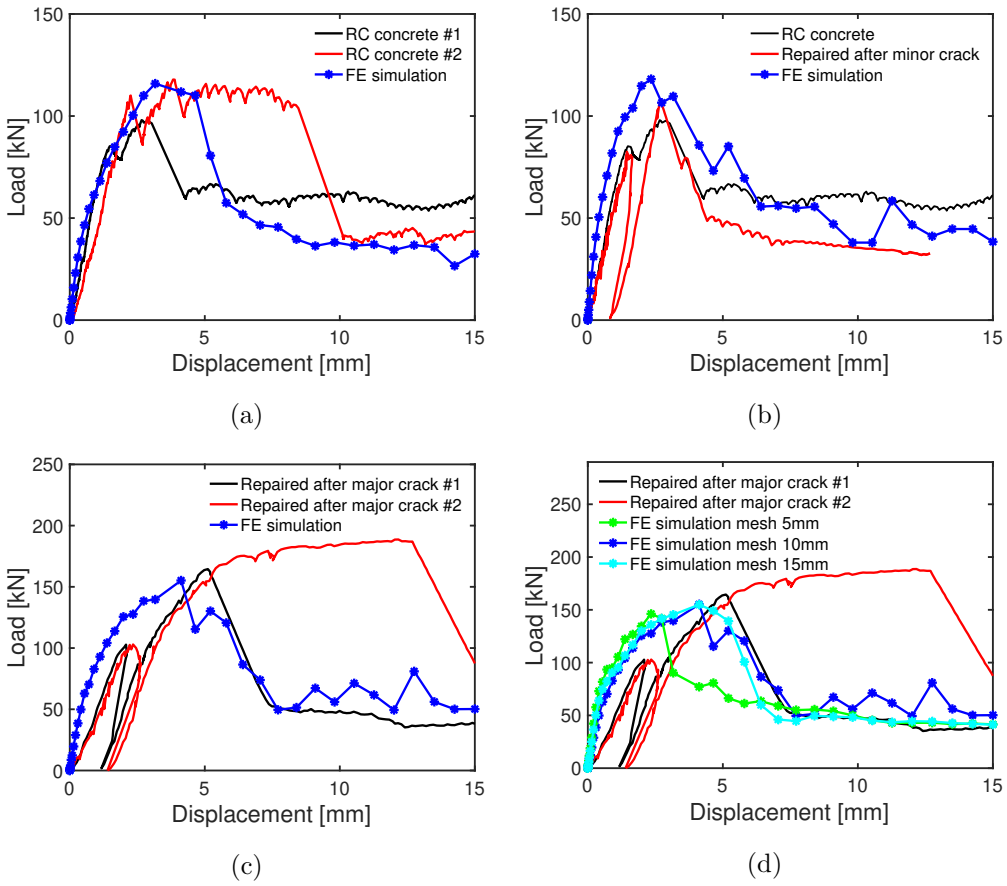

Figure 11: Numerical and experimental load/displacement curves obtained during TPB tests performed on (a) As-built RC beams; (b) Repaired RC beams with minor cracks; (c) Repaired RC beams with major cracks; (d) Repaired RC beams with major cracks simulated for different mesh sizes.

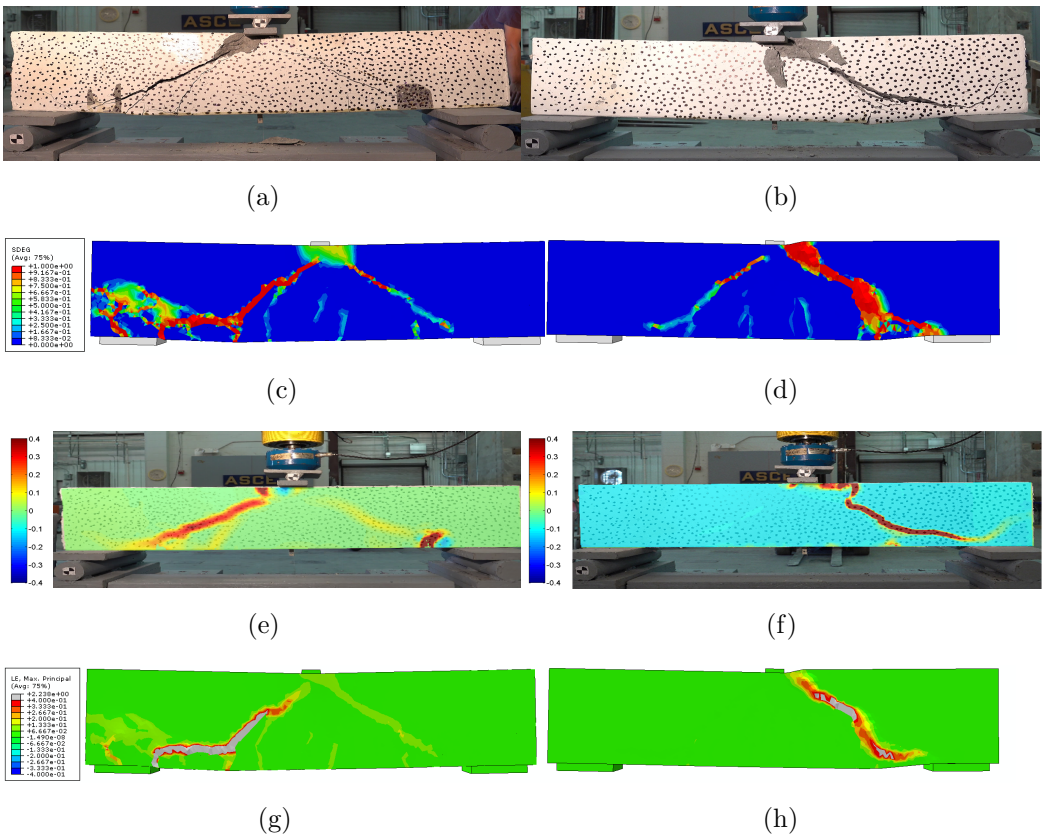

Figure 12: Experiment and simulation results obtained for repaired RC beams: (a) Photograph of repaired RC beam with major cracks; (b) Photograph of repaired RC beam with minor cracks; (c) Snapshot of the FEM mesh, showing the zones of damage at failure for the repaired beam with major cracks; (d) Snapshot of the FEM mesh, showing the zones of damage at failure for the repaired beam with minor cracks; (e) DIC results at failure, showing the field of maximum principal strain in the repaired beam with major cracks; (f) DIC results at failure, showing the field of maximum principal strain in the repaired beam with minor cracks; (g) Snapshot of the FEM mesh, showing the distribution of maximum principal strain at failure in the repaired beam with major cracks; (h) Snapshot of the FEM mesh, showing the distribution of maximum principal strain at failure in the repaired beam with minor cracks.

100 kN, major cracks occurred. We compared the response of the RC beams where only cracks of width above 0.1 mm were repaired to RC beams where cracks of width above 0.05 mm and or above 0.01 mm were repaired. We note that when cracks of width at least 0.01 mm are repaired, the model predicts the load - displacement curve obtained experimentally. When the width threshold is set to a larger value, the model tends to under-predict the strength of the repaired beam (see Figure 13 (c)). For the RC beams loaded up to 80 kN, minor cracks occurred (maximum crack width: 0.036mm). When we simulated the TPB test with a width threshold of 0.1 mm, we verified that the response of the repaired RC beam was similar to that of the as-built RC beam (results are not shown in the figure for brevity). This was expected, since the maximum crack width observed during the experiments at a load of 80 kN was 0.036mm $<$ 0.1 mm. We then compared the response of the RC beams where only cracks of width above 0.01 mm were repaired to RC beams where cracks of width above 0.005 mm were repaired. Results are presented in Figure 13 (d). We note that when cracks of width at least 0.01 mm are repaired, the model predicts the load - displacement curve obtained experimentally. To summarize, our simulation results suggest that HMWM can penetrate cracks of width 0.01 mm and above by gravity.

6. Conclusions

In this paper, we provided a quantitative assessment of concrete repaired by injection of High Molecular Weight Metacrylate (HMWM), which is a type of epoxy commonly used in construction. Since no experimental standard exists to fabricate and test concrete specimens with embedded cracks

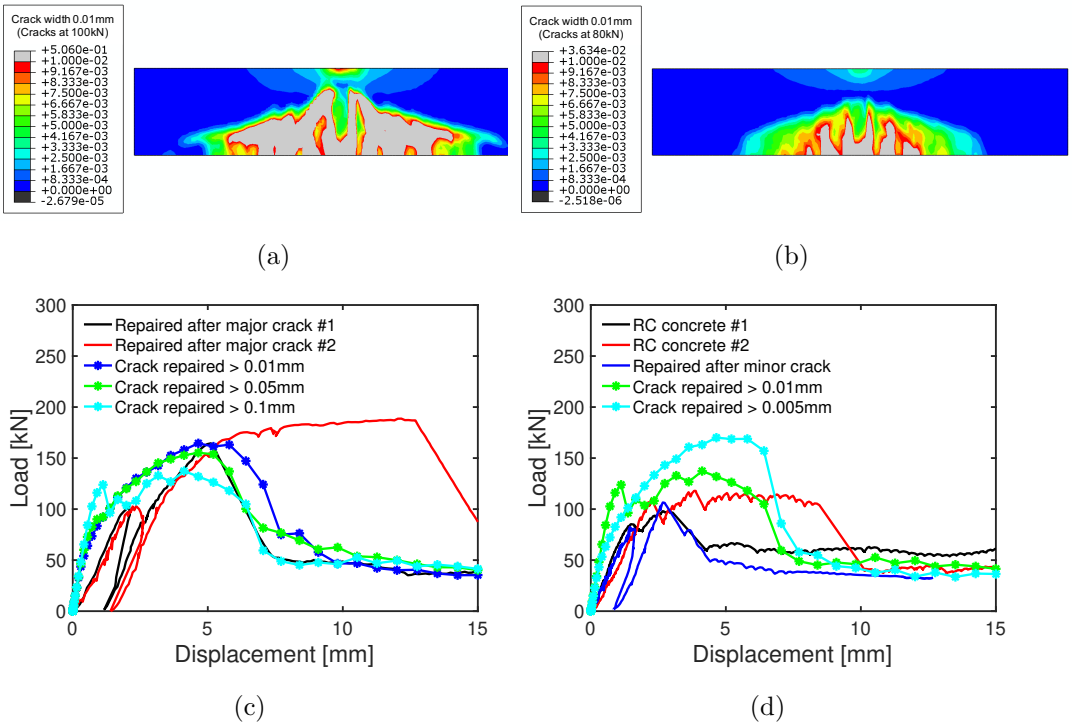

Figure 13: Simulation of the TPB test with RC beams, after repairing cracks of different widths. (a) Maximum load 100kN, crack width threshold 0.01 mm; (b) Maximum load 80kN, crack width threshold 0.01 mm; (c) Load-displacement curve for RC beams loaded up to 100 kN, with repaired cracks of width $>$ 0.01 mm, 0.05 mm, 0.1mm; (d) Load-displacement curve for RC beams loaded up to 80 kN, with repaired cracks of width $>$ 0.005 mm, 0.01 mm.

that are filled with epoxy, novel experimental procedures were established to characterize the mechanical response of repaired concrete. Cut-and-sealed specimens were subjected to uniaxial compression tests and three-point bending tests. The tests were repeatable, i.e. provided similar load-displacement curves with strengths differing in magnitude by 5% or less. Results indicated that repaired concrete specimens had higher stiffness and higher strength than plain concrete specimens. Additionally, steel-reinforced beams were subjected to three-point bending to produce cracks. The beams were then repaired and reloaded. We used DIC to identify the zones of high maximum principal strain after the first loading cycle.

The experiments were simulated by using an original Finite Element approach. Concrete volume elements were assigned a constitutive model that combines continuum damage and plasticity, while the concrete/HMWM interface was modeled with CZEs with a bilinear softening traction-separation law that allowed mode I, mode II, mode III and mixed mode interface debonding. The advantage of the method proposed here is that it requires few experimental results for calibration. The paper reports a detailed procedure to calibrate the model parameters against uniaxial compression tests, which was validated against simulations of three-point bending tests. It is important to note that the model predictions were in agreement with experimental results for both plain and reinforced beams, at both macroscopic scale (load-displacement curves) and at the local scale. For instance, the distribution of damage and the field of maximum principal strain calculated numerically at failure match the damage zone and the maximum principal strain field found experimentally.

When simulating three-point bending tests on repaired reinforced beams, we compared the results obtained when all cracks were repaired vs. only cracks of a minimum width were repaired. Numerical results matched the experimental ones when the cracks with at least 0.01 mm in width were filled with epoxy. Hence, our simulation results suggest that HMWM can penetrate cracks of width 0.01 mm and above by gravity. We also found that HMWM reparation increases concrete stiffness and strength if crack in concrete members are over 0.1 mm in width, in which case, the load capacity of repaired RC beams is 30 to 40% higher than that of as-built RC beams.

Acknowledgements

Support for this research was provided by the Georgia Department of Transportation, as part of the project entitled "Mechanical integrity and sustainability of pre-stressed concrete bridge girders repaired by epoxy injection" (RP 16-24, RP 17-08 and RP 17-12).

References

[1] A. C. Institute, A. C. 224, Control of Cracking in Concrete Structures-ACI 224R-01, American Concrete Institute-ACI, 2001.

[2] T. D. Biel, H. Lee, Performance study of portland cement concrete pavement joint sealants, Journal of transportation engineering 123 (5) (1997) 398–404.

[3] D. Snoeck, K. Van Tittelboom, N. De Belie, S. Steuperaert, P. Dubruel, The use of superabsorbent polymers as a crack sealing and crack healing

mechanism in cementitious materials, in: 3rd International conference on concrete repair, rehabilitation and retrofitting, Cape Town, 2012, pp. 152–157.

[4] C. M. Dry, Repair and prevention of damage due to transverse shrinkage cracks in bridge decks, in: Smart Structures and Materials 1999: Smart Systems for Bridges, Structures, and Highways, Vol. 3671, International Society for Optics and Photonics, 1999, pp. 253–256.

[5] C. Dry, Three designs for the internal release of sealants, adhesives, and waterproofing chemicals into concrete to reduce permeability, Cement and Concrete Research 30 (12) (2000) 1969–1977.

[6] R. L. Wohl, R. W. LaFraugh, Criteria for the selection of penetrating hydrophobic sealers used in the repair of concrete parking decks, in: Building Deck Waterproofing, ASTM International, 1990.

[7] W. D. Mangum, A. J. Bermudez-Goldman, D. Whitney, D. Fowler, A. H. Meyer, Repairing cracks in portland cement concrete using polymers, Center for Transportation Research, The University of Texas at Austin, Report (385-2F) (1986).

[8] R. E. Weyers, B. D. Prowell, M. M. Sprinkel, M. Vorster, Concrete bridge protection, repair, and rehabilitation relative to reinforcement corrosion: A methods application manual, Contract 100 (1993) 103.

[9] M. M. Sprinkel, A. R. Sellars, R. E. Weyers, Rapid concrete bridge deck protection, repair and rehabilitation, Contract 100 (1993) 103.

[10] M. M. Sprinkel, C. D. Moen, et al., Repair and protection of hydraulic cement concrete bridge decks., Tech. rep., Virginia Transportation Research Council (1994).

[11] U. Attanayake, X. Liang, S. Ng, H. Aktan, Penetrating sealants for concrete bridge decks—selection procedure, Journal of Bridge Engineering 11 (5) (2006) 533–540.

[12] K. Johnson, A. E. Schultz, C. French, J. Reneson, Crack and concrete deck sealant performance (2009).

[13] A. Rahim, D. Jansen, N. Abo-Shadi, J. Simek, Overview of high-molecular-weight methacrylate for sealing cracks in concrete bridge decks, Transportation research record 2202 (1) (2010) 77–81.

[14] A. R. Hayes, The evaluation of high molecular weight methacrylate as a treatment option for shrinkage cracks, Tech. rep., Air Force Institute of Technology Wright (2019).

[15] Y.-c. Liang, Experimental study and theoretical modeling of recycled aggregate concrete and evaluation of long-term performance of reinforced concrete bridge decks, Ph.D. thesis, University of Colorado at Boulder (2012).

[16] C. A. Issa, P. Debs, Experimental study of epoxy repairing of cracks in concrete, Construction and Building Materials 21 (1) (2007) 157–163.

[17] I. Basunbul, A. Gubati, G. Al-Sulaimani, M. Baluch, Repaired reinforced concrete beams, Materials Journal 87 (4) (1990) 348–354.

[18] C. Dry, M. Corsaw, E. Bayer, A comparison of internal self-repair with resin injection in repair of concrete, Journal of adhesion science and technology 17 (1) (2003) 79–89.

[19] G. D. of Transportation, Bridge and Structures Design Manual (2015).

[20] D. A. Meggers, Final report crack sealing and repair of older serviceable bridges using polymer sealers, no. January 130 (1998).

[21] C. Rocco, G. Guinea, J. Planas, M. Elices, Review of the splitting-test standards from a fracture mechanics point of view, Cement and concrete research 31 (1) (2001) 73–82.

[22] M. Elices, G. Guinea, J. Gomez, J. Planas, The cohesive zone model: advantages, limitations and challenges, Engineering fracture mechanics 69 (2) (2002) 137–163.

[23] C. A. Coronado, M. M. Lopez, Experimental characterization of concrete-epoxy interfaces, Journal of Materials in Civil Engineering 20 (4) (2008) 303–312.

[24] J. B. Mander, M. J. Priestley, R. Park, Theoretical stress-strain model for confined concrete, Journal of structural engineering 114 (8) (1988) 1804–1826.

[25] K. Park, K. Ha, H. Choi, C. Lee, Prediction of interfacial fracture between concrete and fiber reinforced polymer (FRP) by using cohesive zone modeling, Cement and Concrete Composites 63 (2015) 122–131. doi:10.1016/j.cemconcomp.2015.07.008.

[26] A. Hillerborg, M. Modéer, P.-E. Petersson, Analysis of crack formation and crack growth in concrete by means of fracture mechanics and finite elements, Cement and concrete research 6 (6) (1976) 773–781.

[27] J. Blaber, B. Adair, A. Antoniou, Ncorr: open-source 2d digital image correlation matlab software, Experimental Mechanics 55 (6) (2015) 1105–1122.

[28] H.-H. Choi, S.-M. Hwang, Y. Kang, J. Kim, B. Kang, Comparison of implicit and explicit finite-element methods for the hydroforming process of an automobile lower arm, The International Journal of Advanced Manufacturing Technology 20 (6) (2002) 407–413.

[29] W. Chung, J. Cho, T. Belytschko, On the dynamic effects of explicit fem in sheet metal forming analysis, Engineering Computations (1998).

[30] J. Lubliner, J. Oliver, S. Oller, E. Oñate, A plastic-damage model for concrete, International Journal of solids and structures 25 (3) (1989) 299–326.

[31] J. Lee, G. L. Fenves, Plastic-damage model for cyclic loading of concrete structures, Journal of engineering mechanics 124 (8) (1998) 892–900.

[32] P.-E. Petersson, Crack growth and development of fracture zones in plain concrete and similar materials (1981).

[33] A. S. Genikomsou, M. A. Polak, Finite element analysis of punching shear of concrete slabs using damaged plasticity model in abaqus, Engineering Structures 98 (2015) 38–48.

[34] Z. P. Bažant, E. Becq-Giraudon, Statistical prediction of fracture parameters of concrete and implications for choice of testing standard, Cement and concrete research 32 (4) (2002) 529–556.

[35] J. Martin, J. Stanton, N. Mitra, L. N. Lowes, Experimental testing to determine concrete fracture energy using simple laboratory test setup, ACI Materials Journal 104 (6) (2007) 575.

[36] C. A. Coronado, M. A. Lopez, Experimental characterization of concrete-epoxy interfaces, Journal of Materials in Civil Engineering 20 (4) (2008) 303–312. doi:10.1061/(ASCE)0899-1561(2008)20:4(303).

[37] P. Okumus, M. G. Oliva, S. Becker, Nonlinear finite element modeling of cracking at ends of pretensioned bridge girders, Engineering Structures 40 (2012) 267–275. doi:10.1016/j.engstruct.2012.02.033.
URL http://dx.doi.org/10.1016/j.engstruct.2012.02.033

[38] T. Jankowiak, T. Lodygowski, Identification of parameters of concrete damage plasticity constitutive model, Foundations of civil and environmental engineering 6 (1) (2005) 53–69.

[39] M. Labibzadeh, M. Zakeri, A. A. Shoaib, A new method for cdp input parameter identification of the abaqus software guaranteeing uniqueness and precision, International Journal of Structural Integrity (2017).

[40] O. Yapar, P. Basu, N. Nordendale, Accurate finite element modeling of pretensioned prestressed concrete beams, Engineering Structures 101 (2015) 163–178.

[41] S. Seok, G. Haikal, J. A. Ramirez, L. N. Lowes, High-resolution finite element modeling for bond in high-strength concrete beam, Engineering Structures 173 (2018) 918–932.

[42] J. Lubliner, J. Oliver, S. Oller, E. Oñate, A plastic-damage model for concrete, International Journal of Solids and Structures 25 (3) (1989) 299–326. doi:10.1016/0020-7683(89)90050-4.

[43] A. Turon, C. G. Davila, P. P. Camanho, J. Costa, An engineering solution for mesh size effects in the simulation of delamination using cohesive zone models, Engineering fracture mechanics 74 (10) (2007) 1665–1682.

[44] W. Jin, H. Xu, C. Arson, S. Busetti, Computational model coupling mode ii discrete fracture propagation with continuum damage zone evolution, International Journal for Numerical and Analytical Methods in Geomechanics 41 (2) (2017) 223–250.

[45] J. Edward M. Wu R. C. Router, Crack Extension in Fiberglass Reinforced Plastics, University of Illinois. T. & AM Re (1965).

[46] D. S. Simulia, Abaqus 6.12 documentation, Providence, Rhode Island, US 261 (2012).

[47] B. Standard, 5975: 1996, Code of practice for falsework (1996).

[48] P. P. Camanho, C. G. Dávila, Mixed-mode decohesion finite elements for the simulation of delamination in composite materials (2002).

[49] K. Park, Concrete fracture mechanics and size effect using a special-

ized cohesive zone model, Ph.D. thesis, University of Illinois at Urbana-Champaign (2005).

[50] T. J. Truster, Discontinuous element insertion algorithm, Advances in Engineering Software (2015).

[51] G. Schreppers, C. Frissen, H. Kang, Prediction of crack-width and crack-pattern, TNO DIANA BV, Netherlands (2011).

[52] P. Okumus, M. G. Oliva, S. Becker, Nonlinear finite element modeling of cracking at ends of pretensioned bridge girders, Engineering Structures 40 (2012) 267–275.